Phenomenal Effect of Stable (Ti, Mo)C Nano-Sized Precipitates in Retarding the Recrystallization and Grain Growth in High-Strength Ferritic Steel

PRANABANANDA MODAK, ARKA MANDAL, RICHA GUPTA, ANISH KARMAKAR, SUDIP KUMAR SARKAR, SARITA AHLAWAT, ARUNANSU HALDAR, RAHUL MITRA, SUMAN NEOGY, ANIRUDDHA BISWAS, and DEBALAY CHAKRABARTI

The present study demonstrates remarkable retardation of recrystallization and grain growth during sub-critical annealing of 60 pct cold-rolled ferritic steel containing Ti and Mo. The evolution of Ti–Mo–C based clusters and nano-sized (Ti, Mo)C precipitates during the course of annealing in Ti–Mo added steel was studied extensively through transmission electron microscopy and atom probe tomography. The recrystallization kinetics was evaluated from the electron back-scattered diffraction analysis. The Ti–Mo added steel exhibited just a partially recrystallized (60 pct) fine ferrite grain structure ($\sim$ 8.8 μm) even after annealing for 24 h at 873 K (600 °C). An intriguing aspect was the emergence of tiny partially coherent (Ti, Mo)C precipitates in Ti–Mo steel after 8 hours of annealing. Those precipitates effectively pinned down the dislocations and migrating ferrite boundaries, significantly retarding the recrystallization and grain growth, respectively. Grain refinement and substantial precipitation strengthening from the partially coherent (Ti, Mo)C nano-sized precipitates ensured a decent combination of strength (UTS $\sim$ 821 MPa) and ductility ($\sim$ 16.5 pct total elongation) in the 8 hours annealed sample. Extensive yield point elongation ($\sim$ 4 pct) observed in that sample (undesired for automotive body application) can be attributed to the combined effect of shearing of nano-sized partially coherent precipitates by the dislocations along with Cottrell locking of dislocations by the solute atoms.

I. INTRODUCTION

COLD-ROLLED and annealed sheet steels are extensively exploited for manufacturing automotive body parts owing to their excellent combination of strength and ductility.[1,2] The higher the strength, the lower the section thickness and the associated weight of the automobile can be, improving fuel efficiency and the corresponding environmental impact. Around the globe, there is a continuous drive to design high-strength cold-rolled steel sheets with superior ductility and formability, without compromising the weldability.[3,4]

Among different strengthening mechanisms, grain refinement has been manifested to be effective in improving both strength and toughness without affecting the other properties.[1,5–8] To develop thin steel sheets with very fine grain structure by cold-rolling and annealing route, various severe plastic deformation strategies have been employed such as accumulative roll bonding and cold rolling of martensite followed by recrystallization annealing.[9,10] Due to various practical challenges, such processing techniques are yet to reach the level of industrial-scale production. Therefore, it is necessary to develop sufficiently fine-grained ferritic steel sheet through conventional industrial processing.[11,12]

Nano-sized precipitation strengthened, fine-grained ferritic steels not only possess high strength but also offer decent formability considering the stretch flange-ability and the hole-expansion coefficient. Single-phase

PRANABANANDA MODAK, ARKA MANDAL, RICHA GUPTA, RAHUL MITRA, and DEBALAY CHAKRABARTI are with the Indian Institute of Technology Kharagpur, Kharagpur, West Bengal, 721302, India. ANISH KARMAKAR is with the Indian Institute of Technology Roorkee, Roorkee, Uttarakhand, 247667, India. Contact e-mail: anish.karmakar@mt.iitr.ac.in SUDIP KUMAR SARKAR, SARITA AHLAWAT, SUMAN NEOGY, and ANIRUDDHA BISWAS are with the Materials Science Division, Bhabha Atomic Research Centre, Trombay, Mumbai 400085, India. ARUNANSU HALDAR is with the Indian Institute of Engineering Science and Technology Shibpur, Howrah, West Bengal, 711103, India.
Manuscript submitted August 29, 2021; accepted November 12, 2021.
Article published online January 3, 2022.

ferritic structure free from the stress concentration sites such as coarse carbide particles and secondary constituents (pearlite, bainite or martensite) is known to provide excellent local elongation without defect generation (or deformation instability).[13,14]

The beneficial effect of adding microalloying elements such as Ti, Nb and V in the ferritic steels has been achieved through grain refinement and precipitation strengthening.[1,15–23] The addition of Mo increases the nucleation of microalloy precipitates by lowering the chemical interfacial energy between the precipitates and the matrix (i.e., decreasing the nucleation energy barrier). Thus, the combined addition of Ti and Mo promotes the nucleation of fine and stable (Ti, Mo)C precipitates in ferritic steels.[24–27] The addition of Mo in Ti-containing steel also reduces the coarsening rate of (Ti, Mo)C precipitates.[28–31]

The studies conducted so far on Ti–Mo steels have primarily investigated the evolution of (Ti, Mo)C during hot-deformation processing (i.e., thermomechanical processing) and/or isothermal holding [typically over 873 K to 973 K (600 °C to 700 °C)].[14,26,28–49] Although hot deformation below the austenite recrystallization temperature [~1173 K to 1223 K (~900 °C to 950 °C)] helps in grain refinement, the defects generated in austenite lead to a somewhat limited coarsening of strain-induced precipitates.[32,34,38,49] The temperature and duration of isothermal holding determines the nature (interphase precipitation or random precipitation) and size distribution of (Ti, Mo)C, as reported in earlier studies.[26,33,44,45] Atom clustering plays a crucial role in (Ti, Mo)C precipitation as it occurs through a gradual transformation first from embryo cluster to coherent G-P cluster, then to the NaCl-structured coherent nano-sized precipitates and finally incoherent precipitates.[30,35,40,47] Regarding the mechanical properties, cluster hardening (by the clustering-induced matrix strain) along with precipitation strengthening contributes as much as 300 MPa strength to the hot-rolled Ti–Mo ferritic steels.[33,37,40,42,46,49]

The interest of the present study is to explore the possibilities of developing high-strength formable grades of Ti–Mo-containing steels via cold-rolling and annealing route, considering the requirements for auto body structural applications. Although the automotive sheet steels are processed via cold-rolling and annealing route, the evolution of microstructure and (Ti, Mo)C precipitates during such processing has hardly been investigated in Ti–Mo ferritic steel. The post-cold-rolling annealing treatment often leads to both grain growth and precipitate coarsening, which reduces the strength of conventional microalloyed steels. The significant precipitation of nano-sized partially coherent (Ti, Mo)C and its slow coarsening kinetics to ensure an attractive combination of different tensile properties have been investigated in this study. Although several studies have reported the tensile properties of Ti–Mo ferritic steels, the yield point phenomenon has not been analyzed adequately.[14,33,37,42,46] Yield point phenomenon can be observed in some of the tensile curves reported in the literature on Ti–Mo ferritic steels.[49] Such a phenomenon is not desirable, as it creates stretcher strain during the cold-forming operation and thus affects the surface finish of the automotive sheet. How the alloying elements in solution, the atom clusters and the nano-sized precipitates influence the mechanical properties needs to be understood. These areas have also been addressed in the current study.

II. EXPERIMENTAL DETAILS

A Ti and Mo added microalloyed ferritic steel was chosen for the present investigation. The nominal chemical composition was determined by optical emission spectroscopy analysis (Table I). The steel was industrially processed under the following conditions: soaking at 1473 K (1200 °C) for 1 hours, hot rolling up to a finish rolling temperature of 1073 K (800 °C) followed by forced-air cooling to ambient temperature at a rate varying over the range of 5 to 10 K/s (5 to 10 °C/s). The hot-rolled and air-cooled plate [henceforth referred to as 'as-received' (AR)] was cold rolled (60 pct thickness reduction) to 3 mm thickness and subjected to sub-critical annealing at 600 °C for 2 to 24 hours, as shown schematically in Figure 1. The critical temperatures such as A_{e1} and A_{e3} were predicted from Thermo-Calc® software using TCFE6 database.

Microstructural characterizations were performed using scanning and transmission electron microscopy (SEM and TEM) and electron backscattered diffraction (EBSD) techniques. Samples for SEM were etched using 2 pct Nital solution. TEM samples were prepared by twin-jet electropolishing with 90 vol pct methanol and 10 vol pct perchloric acid at 20 V and 226 K (− 47 °C). TEM examination was performed in JEOL® 2000FX, JEOL® 3010 and Libra® 200FE microscopes. Precipitate size, volume fraction and ferrite grain size were estimated from TEM and SEM micrographs, respectively, using LEICA-MW® image analysis software, following the method suggested by Chakrabarti et al.[50]

Samples for EBSD were prepared by mechanical polishing, followed by electropolishing at 20 V for 15 seconds using an electrolyte containing 80 vol pct methanol and 20 vol pct perchloric acid. EBSD scans were performed on the rolling plane using an Oxford HKL Channel 5 system (Oxford Instruments, Oxfordshire, UK) attached to a Zeiss® Auriga compact SEM. An area of 250 μm × 200 μm from each sample was scanned at a step size of 0.1 μm, with > 95 pct accuracy of indexing. Considering the angular resolution of EBSD, a minimum misorientation threshold of 2 deg was set for the analysis. The boundaries between 2 and 15 deg misorientation and the boundaries > 15 deg misorientation are identified as low-angle boundaries (LAB), i.e., 'sub-boundaries' and high-angle boundaries (HAB), i.e., 'grain boundaries', respectively.

Atom probe tomography (APT) specimens were machined from the bulk samples to the dimension: 0.3 mm × 0.3 mm × 8 mm and subsequently electropolished in two stages using 10 vol pct perchloric acid in methanol and 2 vol pct perchloric acid in butoxyethanol. APT experiments were carried out with UV laser energy ~ 20 nJ at 30 K (− 243 °C) under ultrahigh

Table I. Nominal Chemical Composition (Wt pct) of the Investigated Steel

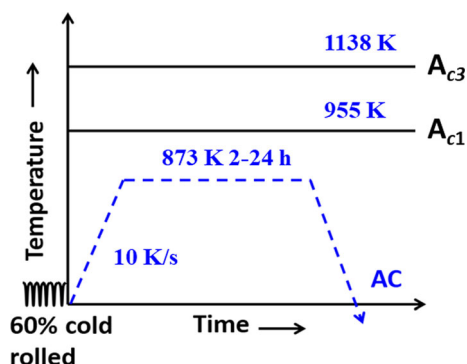| Sample	C	Si	Mn	P	S	Ti	Al	Mo	N	Fe
Ti–Mo Steel	0.06	0.221	1.4	0.012	0.006	0.083	0.051	0.22	0.003	bal.

Fig. 1—Schematic diagram showing the cold-rolling and annealing schedule; AC: air cooling.

vacuum ~ 1.5E-10 mbar, using a CAMECA® FlexTAP instrument. Field ion microscopy (FIM) was performed at 30 K (− 243 °C) under neon pressure of 1.0E-5 mbar using the same CAMECA® FlexTAP instrument. Analysis of the tomographic data was performed using IVAS 3.8 software. The data were reconstructed using a voltage-based protocol with the evaporation field of 33 V/nm and a detector efficiency of 62 pct. The k-factor and image compression factor (ICF) were 6.7 and 1.6, respectively. Carbon is known to field evaporate both as mono-atomic and molecular ions,[51] and indexing of carbon peaks in the mass spectrum was done accordingly. Peaks at the following mass to charge state ratios (m/n), 6, 6.5, 12, 13 Da, were indexed as mono-atomic carbon ions, whereas the peaks at 18 and 18.5 Da were assigned to tri-atomic carbon ions.[51,52] Cluster search analysis by maximum separation envelope method[53] with an order of 3 (Ti, Mo and C atoms) was conducted using the following parameters: $d_{max} = 0.7$ nm, $N_{min} = 10$ atoms, $L = 0.55$ nm and $d_{erosion} = 0.55$ nm. Clusters containing < 20 atoms were ignored for further analysis. Compositions of all the precipitates were determined using proximity histogram technique. An average of five data points at the center of the precipitate denoted the precipitate composition. For the matrix composition, an average of ten data points far from the interface was used. The error bar corresponded to the standard deviation from the mean value. Additional details about analysis procedure can be found in the References 54, 55.

Vickers macrohardness data were obtained at a load of 2 kgf and 15 s dwell time. Instrumented indentation tests were carried out in Anton Paar GmbH Nanoindenter® (Santner Foundation, Austria) with a Berkovich indenter.[56] The maximum load and dwell time used for the test were 25 mN and 10 seconds, respectively. A minimum of ten data points were collected for each condition to ensure statistically reliable analysis. The average values are plotted along with their standard deviations. Tensile samples were prepared following the ASTM E8[57] standard and tested in an Instron® 8800 MK3305 servo-electric test system (250 kN). Tensile tests were performed at room temperature [~298 K (~ 25 °C)] with an initial strain rate of $6.6 \times 10^{-4} s^{-1}$. An extensometer of 25 mm gauge length was used for the accurate measurement of strain.

Dislocation density was calculated from X-ray diffraction data using modified Williamson–Hall method, details of which are given in the "Appendix".

III. RESULTS

The microstructural evolution of the AR plate following cold rolling and subsequent sub-critical annealing has been probed from different angles using suitable characterization techniques, such as grain size (SEM), hardness (macro- and nanoindentation hardness), extent of recrystallization (SEM-EBSD), precipitation (morphology, distribution-TEM; composition-APT), and is reported below accordingly.

A. As-Received (AR) Microstructure

Microstructure of the hot-rolled and air-cooled AR strip, shown in Figure 2(a), consists of ferrite and a small amount (< 5 pct) of cementite. The cementite was present in the form of lamellae as well as distributed spherical particles. The steel consistently had a fine grain structure (grain diameter < 10 μm) with a uniform distribution of cementite particles (0.5 to 1.0 μm) as indicated by red arrows in Figure 2(a). Detailed characterization of a similar grade steel in the hot-rolled (and coiled) condition can be found in the work by Jha et al.[58]

B. Microstructural Evolution During Cold-Rolling and Annealing Treatment

Severe cold rolling led to the formation of pancake-shaped ferrite grains elongated along the rolling direction, as shown in the SEM micrograph in Figure 2(b). Cold rolling also resulted in disintegration and dispersion of cementite lamellae in the form of discrete cementite particles (typical size 100 to 400 nm) within the deformed ferrite matrix, as indicated by red arrows in Figure 2(b). The cementite particles were uniformly distributed in the matrix.

Upon annealing at 873 K (600 °C), the cold-rolled microstructure remained virtually unaltered up to 6 hours (Figures 2(c) and (d)). The microstructural change
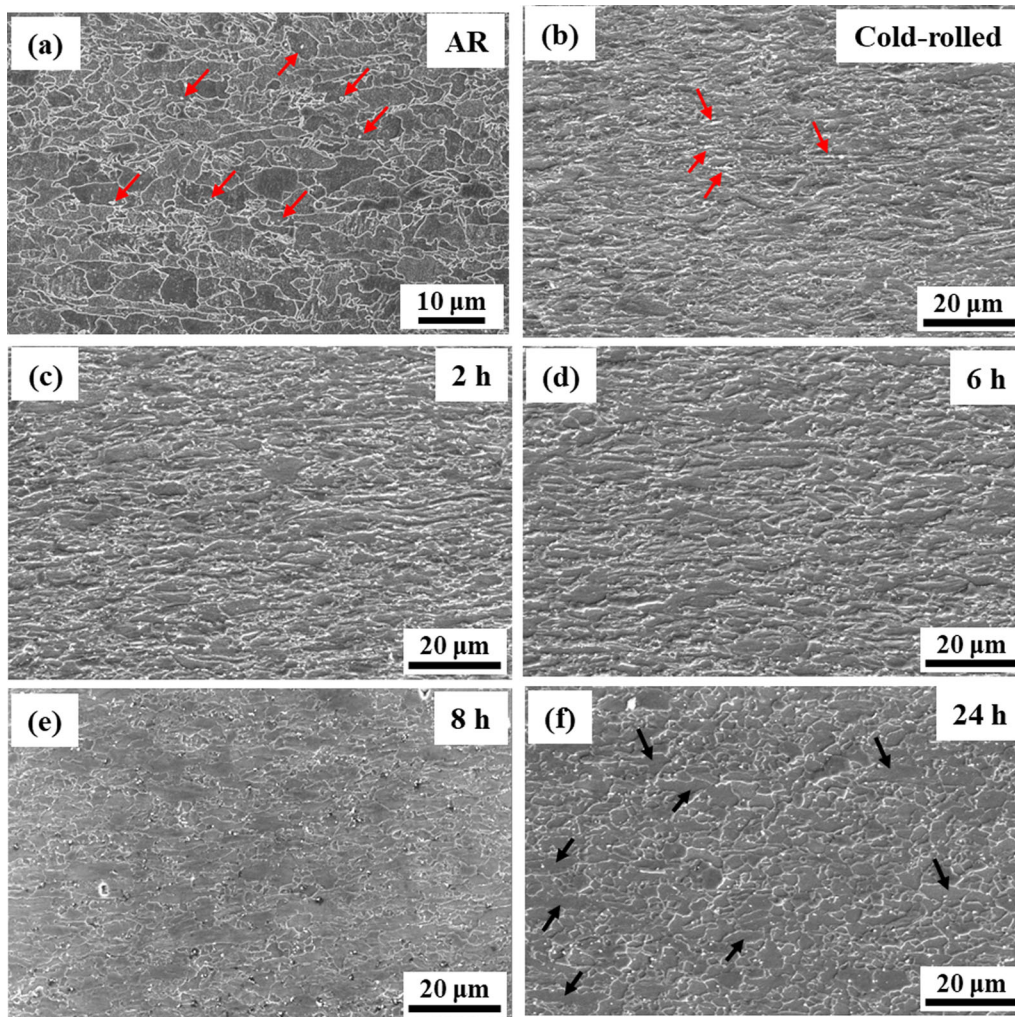
Fig. 2—SEM micrographs of the (*a*) AR, (*b*) cold-rolled and (*c* to *f*) cold-rolled and annealed samples. Cementite particles are indicated by red arrows in (a) and (b); elongated grains shown by black arrows in (f) (Color figure online).

was noticed only on further annealing, as demonstrated by the partially recrystallized fine-grained ferrite matrix after 8 and 24 hours in Figures 2(e) and (f), respectively. Quantitative analysis of recrystallized fraction and grain size is discussed later in Section III–C. Carbide particles at this stage too were homogenously distributed within the matrix. After 24 hours of annealing, the average size of recrystallized ferrite grains was 8.8 $\pm$ 2.3 μm and the carbide particles were in the range of 200 to 500 nm. The average aspect ratio of the elongated grains (indicated by black arrows in Figure 2(f)) was measured as ~ 2.2 $\pm$ 0.15. It is evident that the steel demonstrated a remarkably high resistance to recrystallization and grain growth. Consequently, the steel sample also exhibited a significantly strong resistance to softening, as detailed in the next section.

C. Recrystallization Kinetics

1. Hardness measurement

Macrohardness and nanoindentation hardness tests were conducted on AR, 60 pct cold-rolled and annealed samples and plotted as a function of the annealing time in Figure 3(a). Cold rolling increased the hardness with respect to that of the AR samples in both the measurements. Macrohardness increased from 250 $\pm$ 4 to 355 $\pm$ 4 Hv, whereas the nanoindentation hardness increased from 4.3 $\pm$ 0.21 to 4.6 $\pm$ 0.23 GPa. Three different stages have been observed during annealing in both the hardness profiles, namely (1) Stage I: an initial gradual decrease in hardness up to 6 h, (2) Stage II: marginal increase between 6 to 8 h and (3) Stage III: a gradual decrease beyond 8 h of annealing.
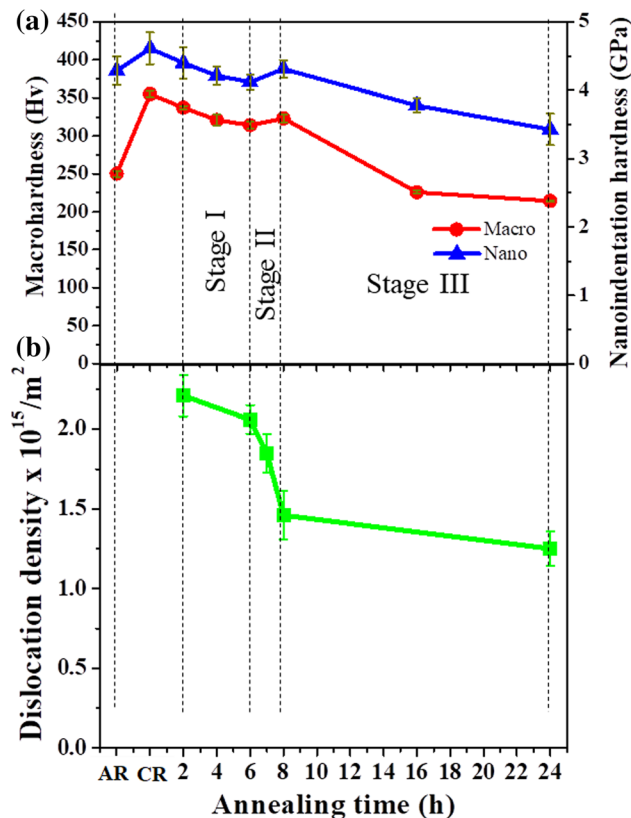
Fig. 3—(*a*) Macrohardness and nanoindentation hardness after hot-rolling, cold rolling and annealing at 873 K (600 °C) for different durations; (*b*) dislocation density calculated from XRD data.

Dislocation densities calculated from the XRD analysis are also shown in Figure 3(b). Despite no reduction in hardness values between 6 and 8 hours of annealing, a significant drop in dislocation density was noticed in this time period. This result also indicates the recovery and recrystallization of the matrix as observed from the SEM results in Figure 2.

2. *EBSD analysis*

Grain orientation spread (GOS) maps obtained from the EBSD analysis of the annealed samples are presented in Figures 4(a) through (e). The GOS associated with a grain is the mean value of the misorientations between all the pixels within the grain and the mean orientation of that particular grain. GOS mapping can thus be a useful tool to display the variation in local strain within the microstructure. The minimum GOS value of < 1 deg in blue indicates strain-free recrystallized grains, whereas the maximum GOS value of 15 deg in red represents the heavily deformed grains. Annealing up to 6 hours resulted only in limited recovery without any considerable recrystallization as evident from the high GOS values (5 to 15 deg) for most of the grains (Figures 4(a) and (b)). Interestingly, the kinetics of recrystallization accelerated after 6 hours of annealing as depicted by a sudden rise in the population of strain-free recrystallized grains in the GOS map in Figure 4(c) corresponding to 7 hours annealing.

Recrystallization process again became sluggish after 8 h of annealing and continued till 24 hours (Figures 4(d) and (e)). Even the 24 hours annealed sample contained some elongated unrecrystallized grains as indicated in Figure 4(e) and exemplified as well in the SEM micrograph in Figure 2(f). The average grain size and aspect ratio of the elongated grains were estimated as ~ 12.1 ± 2.8 μm and 2.0 ± 0.12, respectively. Grain boundary fraction (low-angle and high-angle boundaries) and recrystallization fraction (in terms of GOS) were calculated from the EBSD data to quantify the recrystallization kinetics and are plotted against the annealing time in Figure 4(f). The grains having GOS value of < 1 deg were considered as the recrystallized grains.[59,60] A sudden increase in high-angle grain boundary fraction and recrystallization fraction observed with an increase in the annealing duration from 6 to 8 hours is indicative of accelerated recrystallization (Figure 4(f)). Interestingly, dislocation density calculated using XRD-based method exhibited the same trend but of a different order attributed to the difference in characterization volume and an overall spatial resolution between XRD and EBSD.

D. *Characterization of Precipitates by TEM*

1. *AR, cold rolled and annealed up to 6 h in stage I*

To ascertain the identity, morphology, distribution, size and volume fraction of the precipitates, TEM examination was carried out. The TEM micrographs of AR sample (Figures 5(a) and (b)) and 60 pct cold-rolled sample (Figure 5(c)) show the nano-sized precipitates (< 15 nm in diameter) preferentially located on the dislocation networks (Figures 5(a) and (c)) and boundaries (dark-field image in Figure 5(b)). Selected area electron diffraction (SAED) patterns obtained from the precipitates were indexed and found to represent a face-centered cubic (FCC) crystal structure (provided as inset) (Figures 5(a) through (c)). As the investigated steel was hot-rolled and directly air-cooled, the precipitation was incomplete as evidenced by the low precipitate fraction.

The EDS analysis showed the presence of Ti and Mo within the precipitates (likely to be (Ti, Mo)C) in cold-rolled and annealed samples, as can be seen in the insert in Figure 5(d). Figure 5(e) shows a magnified dark-field image corresponding to a small region of Figure 5(d) indicated by a red square. Quite a few comparatively coarser precipitates (8 to 18 nm in diameter) were detected mainly on the sub-grain boundaries (shown by thick yellow arrows). A few tiny precipitates (2 to 8 nm in diameter) were also found within the grains as indicated by red arrows in Figure 5(e). A high-resolution transmission electron microscopy (HRTEM) image of a relatively coarser precipitate in Figure 5(f) reveals the incoherent nature of the precipitate-matrix interface as indicated by red and black lines. The corresponding fast Fourier transform (FFT) pattern of the image is inserted in Figure 5(f). At this stage too, distribution of the precipitates was found to be non-uniform, and their number density was quite low.
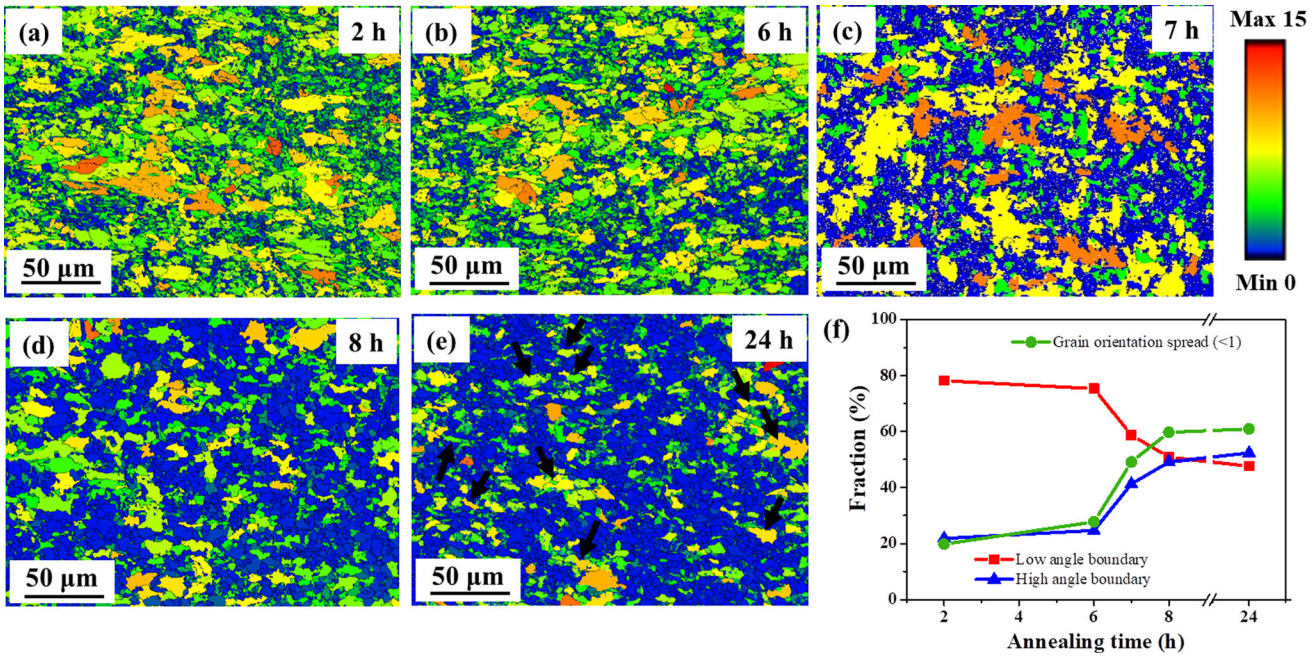
Fig. 4—Grain orientation spread (GOS) maps of the samples annealed at 873 K (600 °C) for (*a*) 2 h, (*b*) 6 h, (*c*) 7 h, (*d*) 8 h and (*e*) 24 h, (f) low- and high-angle boundary fraction (pct) and recrystallized fraction (pct) (GOS < 1 deg) plotted as a function of annealing time.

2. *Annealed for 7 to 8 h in stage II and up to 24 h in stage III*

Results from the TEM investigation carried out on the samples annealed for duration beyond 6 hours are presented in Figure 6. The number of relatively coarser precipitates (10-20 nm), which were observed frequently on the boundaries of 6 hours annealed sample, declined noticeably after 7 hours of annealing as indicated by thick yellow arrows in Figure 6(a). A few tiny precipitates (≤ 8 nm) inside the grain as shown by the red arrows in Figure 6(a) were also noticed in the 7 hours annealed sample. A coherent patch of the interface between one such fine precipitate and the ferrite matrix, as conceivable from the HRTEM image of Figure 6(b), can be considered as the evidence indicating their fresh nucleation. The lattice planes are found to be continuous across the interface as pointed out by a red dotted line in Figure 6(b).

A dramatic increase in the number density of these freshly formed fine precipitates (2 to 5 nm in diameter) was noticed after 8 hours of annealing as specified by the red arrows in Figure 6(c). The corresponding EDS spectrum given as inset suggests the composition of the precipitates as (Ti, Mo)C. The lattice parameter of the precipitates was determined as 0.425 nm from an HRTEM image along the (020) plane (Figure 6(d)). The computed value of the lattice parameter lies within the range reported previously (0.423 to 0.430 nm) for the similar type of precipitates.[14,61] Further annealing up to 24 hours broadened the size range of (Ti, Mo)C precipitates (Figure 6(e)). The 24 hours annealed sample contained both the newly formed fine precipitates (4 to 10 nm), indicated by red arrows in Figure 6(e), and the previously formed coarsened ones (15 to 28 nm), which

are marked by thick yellow arrows in Figure 6(e). This indicates the nucleation of (Ti, Mo)C precipitates till the very end of the annealing operation (24 hours).

3. *Size, volume fraction and number density of the nano-sized precipitates*

Precipitate size, volume fraction and number density are plotted as a function of annealing time in Figure 7(a). The average size of fine precipitates in the cold-rolled sample was calculated as 6 ± 1.8 nm. It can be observed that the average precipitate diameter increased initially from 6.4 ± 1 nm (after 2 h annealing) to 7.7 ± 1.8 nm up to 6 hours of annealing. There was then a marginal decrease in the average precipitate size from 7.7 ± 1.8 nm to 6.9 ± 2 nm between 6 and 8 hours due to the formation of numerous fine precipitates. Again, a gradual increase thereafter in the average size of the precipitates to 10.3 ± 2.5 nm upon 24 hours annealing was recorded. This gradual increase, however, indicated that the amount of coarsening was not significant. The volume fraction of the precipitates was calculated using the expression proposed by Ashby and Ebeling, Eq. [1][62]:

$$f = \frac{\pi}{6} N_P \left(d^2 + s^2 \right) \qquad [1]$$

where d is the mean particle size (diameter), s is the standard deviation of the size distribution, and N_P is the precipitate number density observed per unit area. Volume fraction increases from 0.0014 in the cold-rolled sample to 0.0035 after 24 hours of annealing, Figure 7(a). Number density per unit volume (N_v) was calculated from the volume fraction (f) and the mean radius (r)[63]:
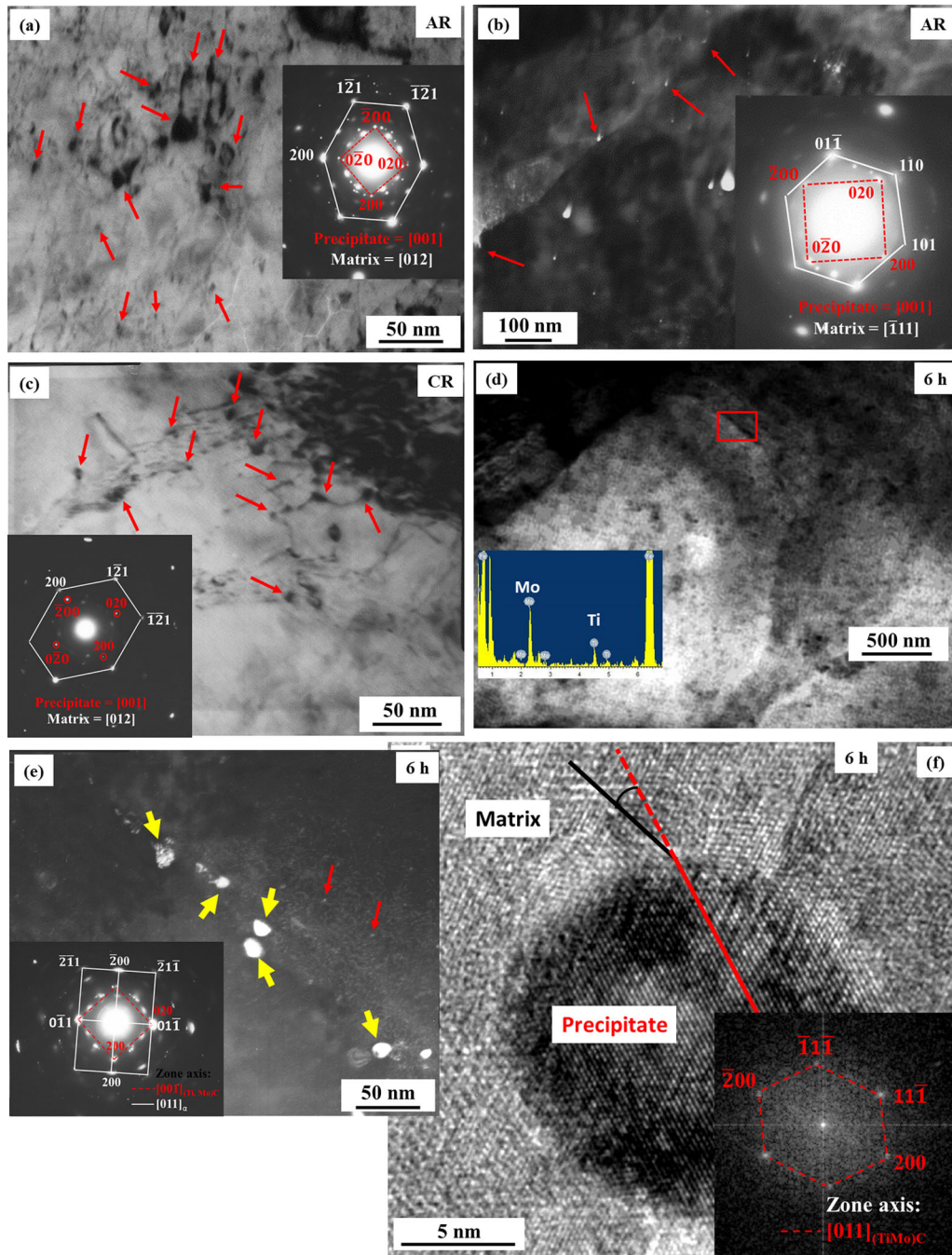
Fig. 5—(*a*) Bright-field TEM micrograph and (*b*) a dark-field TEM micrograph of AR sample (red arrows indicate precipitates); SAED pattern inserted within the figures, (*c*) bright-field TEM micrograph of cold-rolled sample; SAED pattern inserted within the figure, (*d*) bright-field TEM micrograph of the steel annealed at 873 K (600 °C) for 6 h, (*e*) magnified dark-field TEM micrograph of the region indicated in (d), (fine and coarse precipitates are indicated by red and thick yellow arrows, respectively); SAED pattern inserted within the figure, (*f*) HRTEM image of a precipitate from 6 h sample; FFT pattern inserted (Color figure online).

$$N_{\mathrm{v}} = \frac{f}{(4/3)r^3} \qquad [2]$$

A continuous decrease in the number density was observed up to 7 hours of annealing from 1.75×10^{22} m^{-3} in the cold-rolled sample to 1.17×10^{22} m^{-3} in 6 hours annealed sample, Figure 7(a). The number density rose to a maximum after 8 h annealing (1.96×10^{22} m^{-3}) and it reduced again after annealing for 24 hours (0.61×10^{22} m^{-3}). The precipitate size distribution based on number frequency exhibited an apparently bimodal nature (dual peaks are indicated in Figure 7(b)) except in 8 hours sample. Formation of a large number of tiny precipitates (> 5 nm) after 8 hours of annealing resulted in the reduction of second peak significantly with respect to the first one and hence, the dual peak nature
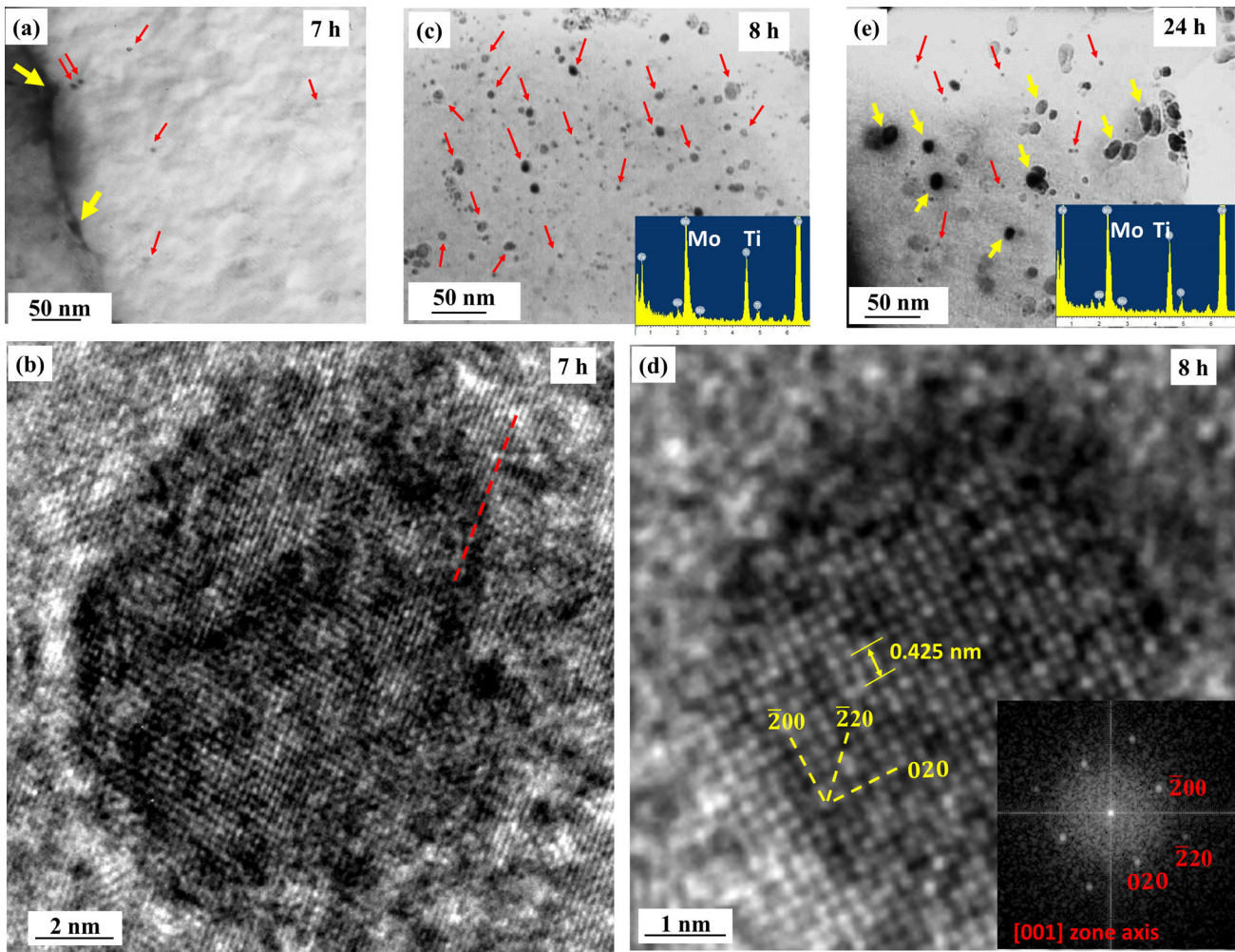
Fig. 6—(a) Bright-field image after 7 h annealing, (b) a magnified HRTEM image from fine precipitate, (c) bright-field image of 8 h annealed sample (EDS spectrum of precipitate inserted), (d) a magnified HRTEM image from fine precipitate shown in (c) (FFT pattern inserted), and (e) bright-field image of 24 h annealed sample (EDS spectrum of precipitate inserted); fine and coarse precipitates are indicated by red and thick yellow arrows, respectively in (a) and (e) (Color figure online).
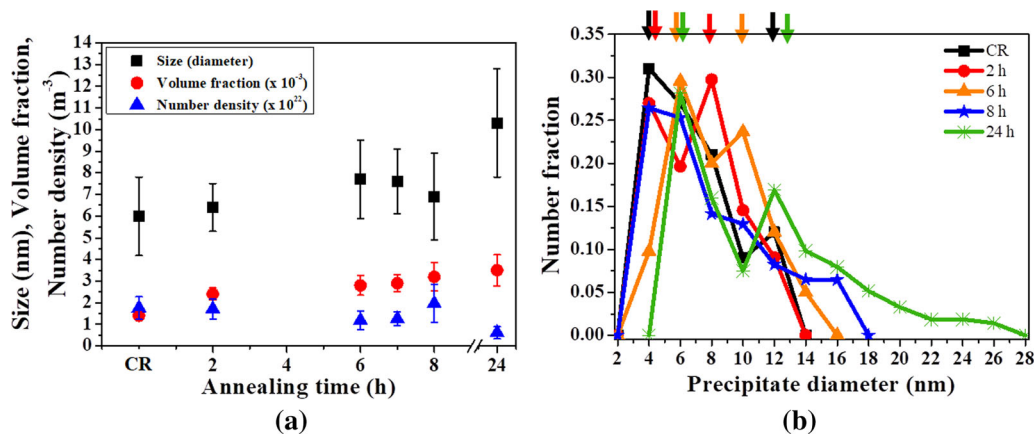

Fig. 7—(a) Precipitate size, volume fraction and number density with annealing time, (b) precipitate size distribution in terms of number fraction at different annealing time. The peaks of the size distributions are indicated by arrows of different colors.

converted to single peak type. The size distribution of the precipitates shifted towards a wider size range from 2 to 14 nm in the cold-rolled sample to 4 to 28 nm in 24 hours sample as the annealing progressed.
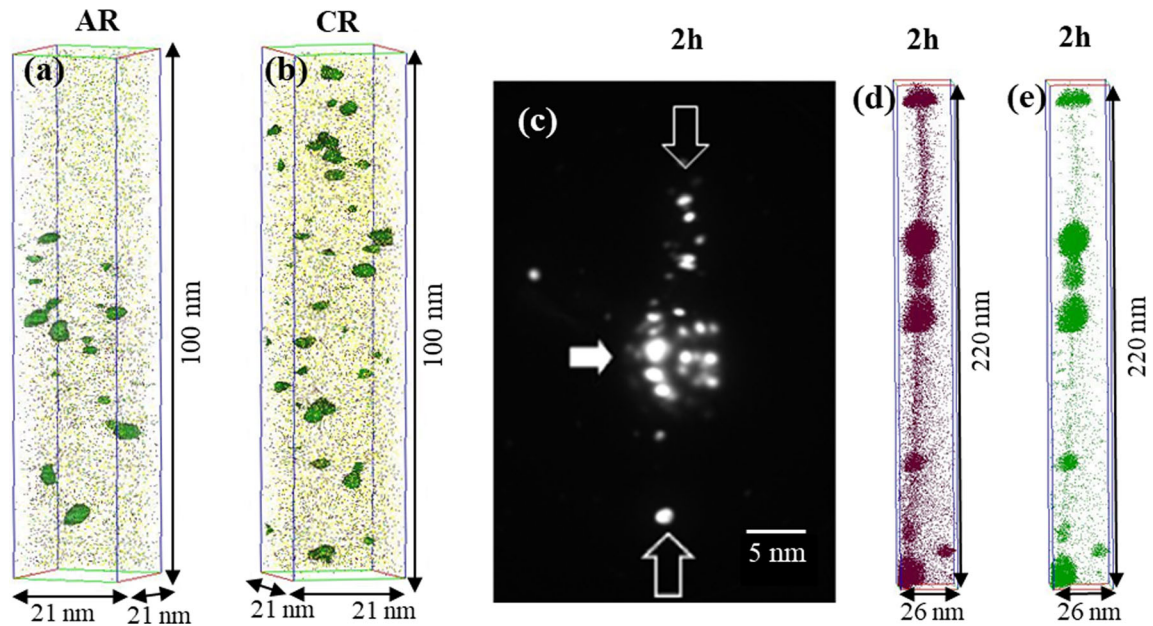
Fig. 8—(*a*) and (*b*) Atom maps containing fine precipitates in as-received (AR) condition and cold-rolled (CR) condition, respectively (bright-field micrograph of the cold-rolled sample depicts the same precipitates in Figure 5c). Only Ti (green), Mo (yellow) and C (brown) atoms are displayed for clarity, and the precipitates are delineated by 1 at. pct Ti iso-concentration surfaces. (*c*) to (*e*) Evidence of grain boundary precipitation after 2 h annealing: (c) an FIM image, where the vertical arrows indicate the grain boundary and the horizontal one marks the precipitate; (d) and (e) atom maps of the very same sample displaying precipitates rich in C (brown) and Ti (green) atoms, respectively (Color figure online).

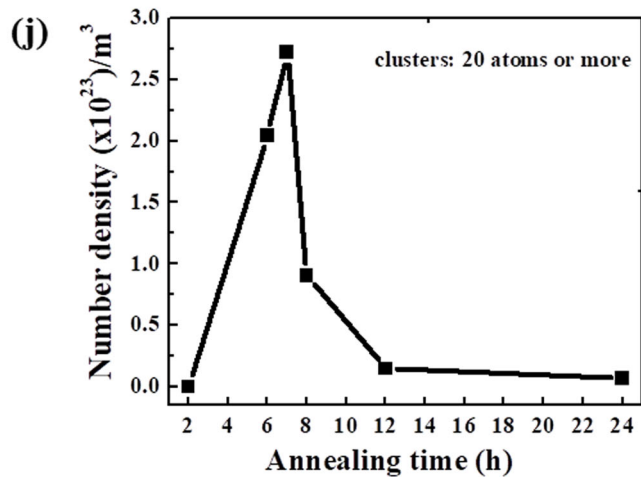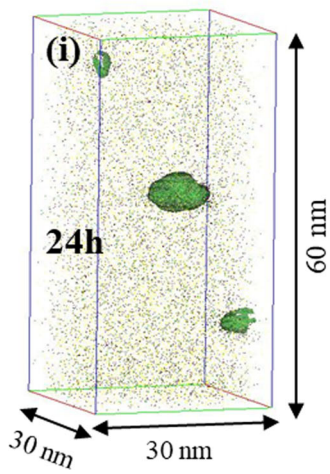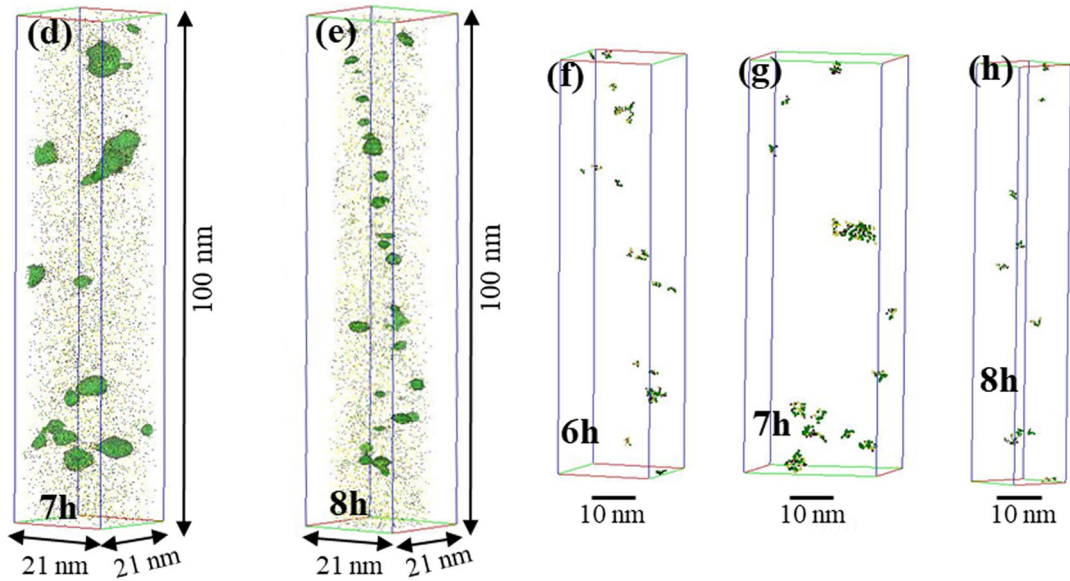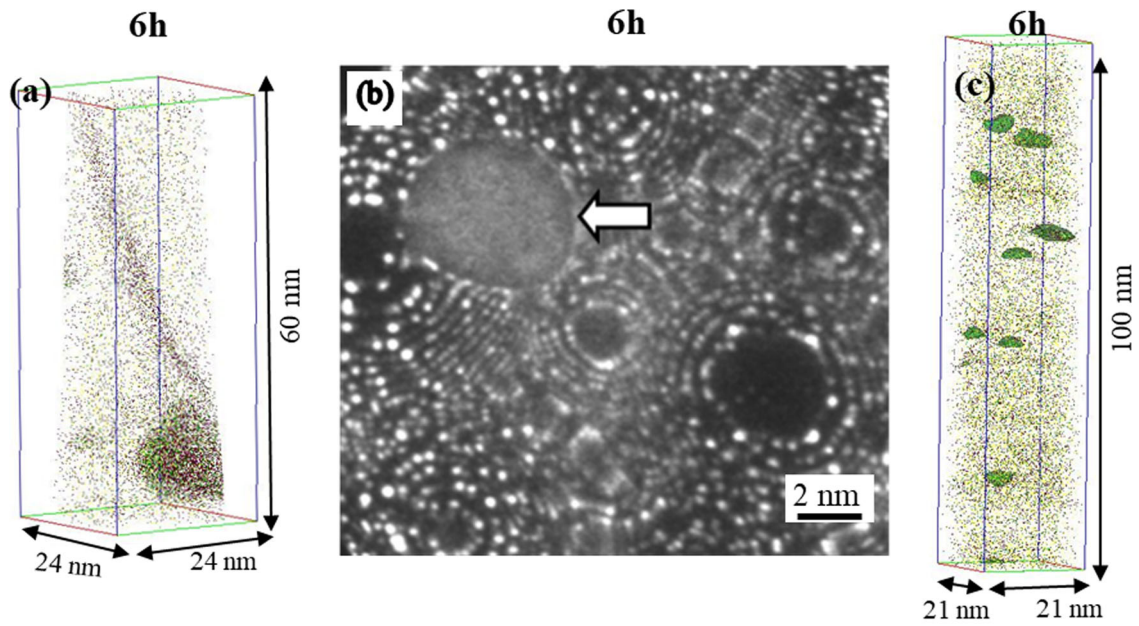### E. *Investigation of nano-sized precipitates and clusters by atom probe tomography (APT)*

To analyze the precipitate compositions, substantiate the results obtained from TEM analysis and comprehend the distribution of precipitates and clusters in 3D space, the aforementioned samples were examined by APT. Different types of precipitates with varied sizes and compositions were detected both before and after annealing as shown in Figures 8 and 9. For clarity, only the most significant solutes, namely, Ti (green), Mo (yellow) and C (brown), are displayed in all the atom maps, except for Figures 8(d) and (e). APT analysis revealed significant partitioning of Ti, Mo and C to the precipitates: iso-concentration surfaces based on any one of these elements help portray the precipitates for better visualization. In all the pertinent cases, 1 at. pct Ti iso-concentration surfaces have been used to delineate the precipitates.

Figures 8 and 9 depict the atom maps and FIM images showing precipitates and clusters in the samples. Both the AR as well as the cold-rolled samples exhibited fine Fe-rich (Ti, Mo)C precipitates (Figures 8(a) and (b)). The precipitates in AR and cold-rolled conditions were found to contain 88.3 ± 0.6 and 84.3 ± 2.4 at. pct Fe, respectively. This marginal reduction in the Fe content after cold rolling was accompanied by a proportionate increase in the Mo-concentration of the precipitates (from 0.6 ± 0.2 to 2.3 ± 0.3 at. pct). Precipitates in Figures 8(a) and (b) are likely to represent those that were imaged earlier by TEM in Figures 5(a) and (c), respectively.

Evidence of grain boundary precipitates after 2 hours annealing is presented in Figures 8(c) through (e); in this case, the very same sample was analyzed by both FIM and APT. Vertically aligned bright spots in the FIM image in Figure 8(c) indicate a grain boundary with considerable solute segregation, which is confirmed by the atom maps in Figures 8(d) and (e). Vertical arrows point at the grain boundary, whereas the horizontal one marks the precipitate (Figure 8(c)). The grain boundary precipitates, which could be detected after annealing for longer durations as well, are shown in Figure 9(a) corresponding to the 6 hours annealed sample. Coarser precipitates with a size range of 10 to 15 nm were mainly concentrated along the grain boundaries, while comparatively finer precipitates with a size range of 2 to 5 nm were distributed within the matrix (Figures 9(b) and (c)). This finding is in accordance with the TEM results. The FIM image in Figure 9(b) shows one such precipitate (marked by arrow) situated within the grain. These types of carbides are known to appear bright in the FIM image.[64] Figures 9(c), through (e) shows precipitates after 6, 7 and 8 hours of annealing, respectively.

Particularly striking was the abundance of fresh fine precipitates formed after annealing for 8 hours, shown in Figure 9(e). This observation is consistent with the TEM image of Figure 6(c). The number density of the fine precipitates (2 to 5 nm) increased remarkably at this stage. Besides, cluster search analysis was performed on all three datasets displayed in Figures 9(c) through (e), after isolating the precipitates. Figures 9(f) through (h) shows the sub-nanometer Ti–Mo–C clusters in the samples annealed for 6, 7 and 8 hours, respectively. Interestingly, the number density of these clusters (with Ti/Mo = 2.6) shows an increase with an increase in annealing duration from 6 to 7 hours and declines after 8 hours of annealing. Subsequently, there is a steady fall

in the number density of clusters to an insignificant value upon further annealing (Figure 9(j)). In addition, the sample after 2 hours annealing did not show any sub-nanometer Ti–Mo–C clusters, and the drop in the number density of these clusters after 8 hours annealing coincided with the abundance of fine precipitates. These clusters were probably the precursors of these freshly formed numerous tiny precipitates after 8 hours annealing. Annealing for 24 hours coarsened the precipitates and reduced their number density (Figure 9(i)). All these findings are in very good agreement with the TEM results.

The elemental distribution as a function of the distance from the matrix to precipitate as well as plots depicting the variations of compositions (in at. pct) of the precipitates and matrix and Ti/Mo ratio of the precipitates with the duration of annealing is presented in Figure 10. Proximity histograms (Figures 10(a) and (b)) were used to represent the concentration profiles of solutes across the precipitate-matrix interfaces of fine (after 8 hours of annealing) and coarse precipitates (after 24 hours of annealing), respectively. The enrichment of Ti and C was more substantial in the coarser precipitates compared to that in the finer ones. As mentioned earlier, fine precipitates (2 to 5 nm) observed in the AR and cold-rolled samples were predominantly Fe-rich (Ti, Mo)C, and contained a limited amount of alloying elements, 5.1 ± 0.3 at. pct Ti and 0.6 ± 0.2 at. pct Mo in AR sample and 6.0 ± 1.4 at. pct Ti and 2.3 ± 0.3 at. pct Mo in the cold-rolled sample (Figure 10(c)). Notably, the Fe content of the extremely fine microalloyed carbides was high because of the interference by the surrounding matrix. Characterization and analysis of the compositional variation inside the precipitate and in the matrix during annealing of a cold-rolled Ti–Mo steel deserve further attention in future. Even though the concentration of Ti remained virtually unchanged, the precipitates found in the 2 hours annealed sample showed a much higher concentration of Mo (18.8 ± 6.9 at. pct), whereas, at the later stages of annealing, the precipitates exhibited a much higher enrichment of Ti (14.6 ± 3.8 at. pct after 6 hours and 18.2 ± 5.8 at. pct after 8 h of annealing) than Mo (Figure 10(c)). In the case of 10 to 15-nm-sized precipitates, the concentration of Ti (19 to 27 at. pct) always remained higher than that of Mo (6 to 21 at. pct) (Figure 10(d)). The concentration of C in these precipitates increased on annealing for durations up to 6 hours and remained practically

unchanged afterwards. No discernible change in either Mo or Ti concentration of the matrix has been noticed after cold-rolling treatment with respect to the AR sample, as the formation of new precipitates is not possible at room temperature (Figure 10(e)). Increase in the C concentration of the ferritic matrix in the cold-rolled sample is due to the dissolution of cementite particles (and possibly a part of pre-existing (Ti, Mo)C alloy carbides as well) during cold rolling. The matrix became depleted of Mo rapidly between 6 to 7 hours of annealing, whereas of Ti and C between 7 and 8 hours. The Ti/Mo ratio was small (~ 0.3) in the fine precipitates during the early stage of annealing (after 2 hours). However, this ratio increased eventually with the enrichment of Ti at the later stages (Ti/Mo = 2.4 and 7.4 after 6 and 8 hours, respectively) (Figure 10(f)). Coarser precipitates revealed the existence of a Ti/Mo ratio > 1 (~ 1.2 to 2.8) throughout the annealing process (Figure 10(f)).

F. *Tensile Properties*

Tensile tests of the samples were carried out to examine the effect of microstructural evolution on the mechanical properties. The trend observed in the engineering stress-strain curves is presented in Figure 11, and the properties listed in Table II indicate a continuous decrease in the ultimate tensile strength (from 1187 MPa to 746 MPa) and increase in the tensile elongation (from 3.6 to 14.5 pct) with the duration of annealing. Interestingly, the 8 hours annealed sample displayed the maximum yield point elongation (~ 4 pct), followed by a considerable uniform elongation (6.2 pct), as well as a post-uniform elongation (6.3 pct).

IV. DISCUSSION

A. *Evolution of Nano-Sized Precipitates*

The steel was soaked at 1473 K (1200 °C) for 1 h and then hot rolled up to 1073 K (800 °C), followed by forced air cooling. Strain-induced precipitation is expected during hot-rolling, and subsequently some precipitates can form during and after the austenite to ferrite transformation because of the lower solubility of the alloying elements in ferrite than in the austenite. Depending on the effective cooling rate, the precipitation during transformation can take place either as interphase precipitates (preferentially during coiling or slow-cooling) or randomly (preferentially under continuous cooling at a relatively higher cooling rate).[65] Since the hot-rolled steel is forced air cooled [5 to 10 K/s (5 to 10 °C/s)], precipitation is expected to be incomplete and random in nature.

The process of cold rolling disintegrated the cementite lamellae into finer particles and partly dissolved the cementite. This event increased the C content in ferrite solution (see Figure 10(e)), which helped in the formation of atom clusters and nano-sized precipitates (2 to 5 nm), enriched with C (Figure 10(c)). This effect was also reported earlier in Reference 35.
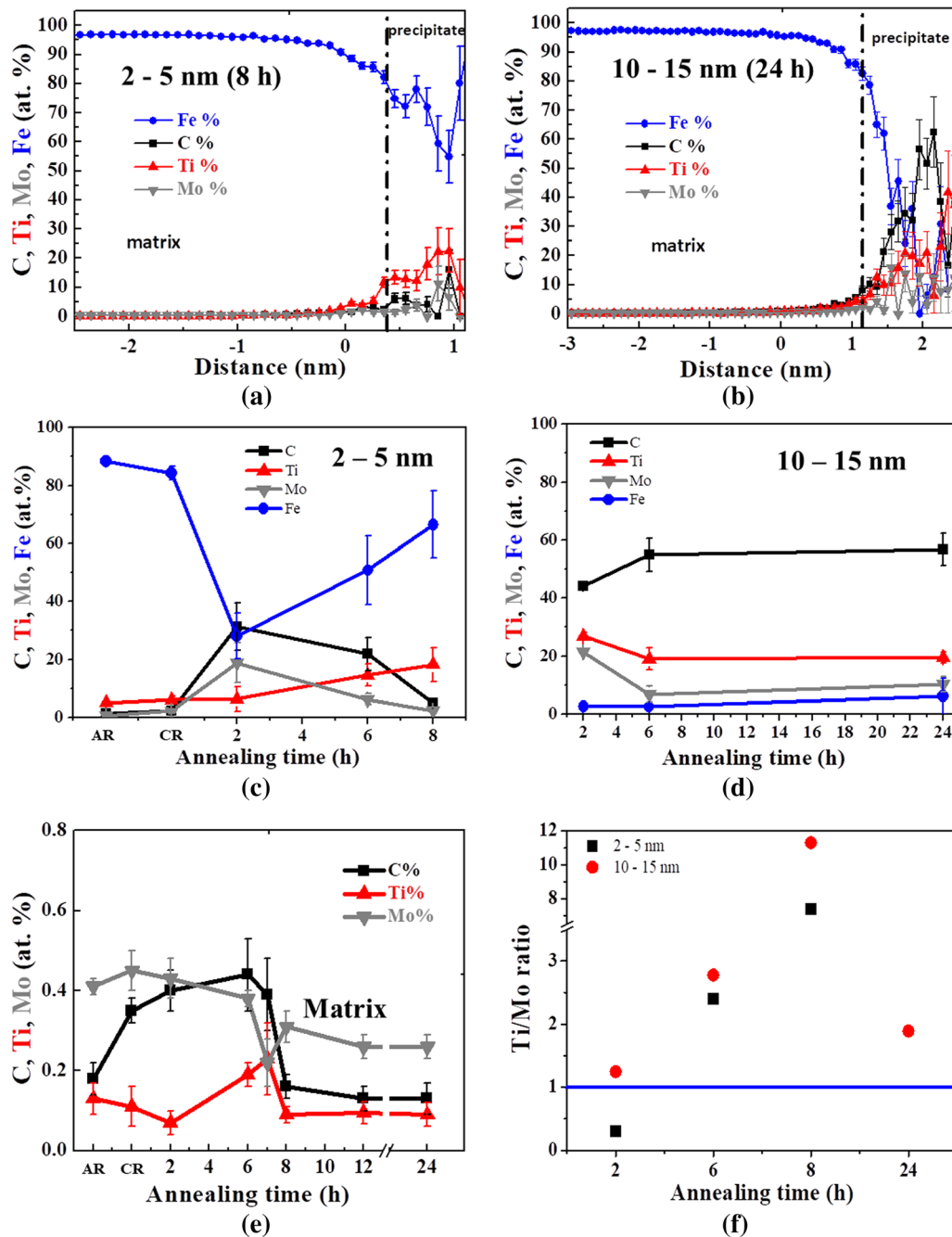
Fig. 10—(a) and (b) Proximity histograms with distance from matrix to precipitate; (c) and (d) composition (at. pct) of (Ti, Mo)C precipitates of 2 to 5 nm and 10 to 15 nm size range, respectively; (e) composition of the matrix (at. pct), (f) Ti/Mo ratio in both types of (Ti, Mo)C precipitates.

It is well known that the rate of nucleation depends strongly on the diffusivity of solute atoms. Therefore, the observed long incubation time (6 to 8 hours) required for the formation of atom clusters and precipitates during annealing can be attributed to the necessity of diffusion of multiple substitutional solute atoms (Mo, Ti and even Fe).[29] Among them, the diffusion of Mo in the BCC iron (which is present in significant quantity in the steel) is known to be the most sluggish (~ 1.5 times slower than Fe and ~ 2.5 times slower than Ti[66]) and hence controls the rate of precipitation. Considering the

volume diffusion of Mo in BCC iron, after 6 to 8 hours of annealing at 873 K (600 °C), Mo atom is expected to diffuse over a distance of 70 to 90 nm, which is similar to the average spacing between the dislocations (70 to 90 nm) and precipitates (40 to 60 nm) in ferrite. Since dislocation pipe diffusion can expedite the process, still, 6 to 8 hours annealing duration was possibly required for the Mo to come out of the dislocations and to form the atom clusters and subsequent precipitates in ferrite. The freshly formed fine precipitates are expected at least to be partially coherent with the ferrite

matrix.[25,30,35,37,39,40] Once the nano-sized precipitates formed, their subsequent growth and coarsening was slow because of the diffusional requirement and the decrease in the Ti concentration in solution. A decrease in the Ti:Mo ratio within the coarsened precipitates from 2.9 after 6 hours annealing to 1.9 after 24 hours annealing justified the depletion of Ti in solution (Figure 10(e)), which reduced further precipitation and, most importantly, restricted the precipitate coarsening.

Several decades ago, Murphy and Whiteman[67] studied the rate of dissolution of Fe_3C and precipitation of Mo_2C during the tempering of martensitic Fe–C–Mo alloy over the range of 773 K to 873 K (500 °C to 600 °C). Although the Mo_2C precipitation started at the dislocations, the precipitation became rapid once the martensite matrix started to recover and the matrix became relatively dislocation free (after around 4.5 hours of tempering). Thus, the delayed precipitation in steel accompanying the microstructural recovery is not a completely new observation. According to the earlier studies, a partial substitution of Mo by Ti within the precipitates reduces the equilibrium concentration of Ti in the matrix, which slows down the diffusion of Ti from the matrix towards the precipitate. The presence of excess C in solid solution also plays the same role.[26,28,30,68,69] In addition, the presence of larger Ti and Mo atoms (atomic radius 1.47 and 1.43 Å,

respectively) in solid solution of Fe (atomic radius 1.27 Å) can increase the effective atomic density and slow down the diffusion further.[70] All these factors in combination could have delayed the precipitation during annealing of the investigated Ti–Mo steel after cold rolling.

A bell-shaped aging curve with respect to aging time or temperature has been widely reported in various microalloyed steels containing V, Nb, Ti, Mo[7,16–18] and even in Ti–Mo steels.[19,20] Most studies on the precipitation of (Ti, Mo)C in low-C ferritic steels have been carried out by either isothermal holding at the temperature range of austenite to ferrite transformation or water-quenching from austenite phase field and aging the martensite structure.[2–5,19,20] In both cases, the driving force for precipitation is very high because of the significant drop in solubility as the austenite transforms into ferrite during isothermal holding, leading to a large supersaturation of alloying elements in the martensite matrix. The precipitation kinetics is further accelerated by the rapid diffusion of Ti and Mo along the austenite-ferrite interface (several hundred times faster than volume diffusion in ferrite) and different boundaries (lath, block-, packet-, and prior-austenite grain boundaries) present in the martensite structure. Therefore, the (Ti, Mo)C precipitation kinetics has been found to be much faster in the earlier studies compared to the present study. In the Ti–Mo alloyed steel, the precipitation of (Ti, Mo)C and the early stage of precipitate growth requires diffusion of both Ti and Mo, which could be matrix diffusion controlled,[2] where, beside the dislocation-pipe diffusion, volume diffusion of Ti and Mo also plays a role.

Regarding the composition of fine precipitates, the results of previous studies suggest that the freshly nucleated (Ti, Mo)C precipitates are richer in Mo than Ti as it reduces the misfit strain between the coherent precipitate and the ferrite matrix and the resultant precipitate-matrix interfacial energy.[25,37] A contradicting observation and hypothesis, however, mentioned that Ti-rich precipitates are formed in the ferrite matrix, initially during the very early stage of aging treatment [only 5 minutes aging at 923 K (650 °C)].[39] Formation of the Ti-rich precipitate is energetically favorable because of the requirement of lower formation energy than that of the Mo-rich counterpart. However, during the initial stage of precipitate growth [after 1 hours
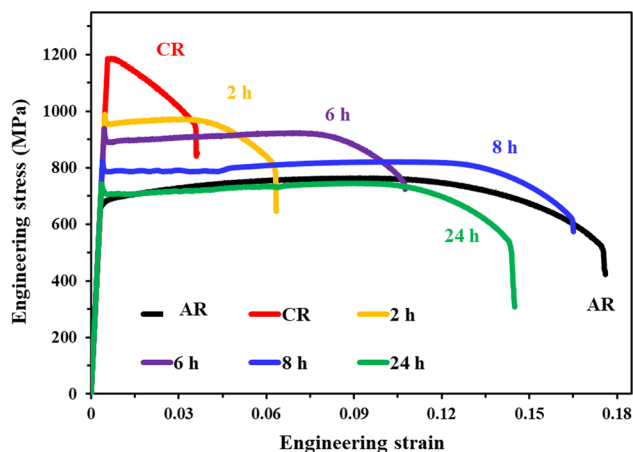

Fig. 11—Engineering stress-strain curves.

Table II. Tensile Properties* of the Steel

Sample	Upper Yield Point (MPa)	Lower Yield Point (MPa)	Yield Point Elongation (Pct)	UTS (MPa)	Uniform Elongation (Pct)[#]	Post-Uniform Elongation (Pct)	Total Elongation (Pct)
AR	657 (yield point only)		—	763	9.2	8.3	17.5
CR	1181 (yield point only)		—	1187	0.8	2.8	3.6
2 h	990	954	0.3	969	3.0	3.2	6.5
6 h	939	890	0.3	924	6.8	3.7	10.8
8 h	823	791	4.0	821	6.2	6.3	16.5
24 h	743	707	0.6	746	8.3	5.6	14.5

*Three specimens were tested for each sample and the deviation was within 5 pct.
#Uniform elongation was calculated from the end of yield point elongation to the point of necking.

aging at 923 K (650 °C)], they become rich in Mo (Ti:Mo ~ 0.9) to reduce the interfacial energy associated with the growth of the disc-shaped (Ti, Mo)C precipitates having a high surface-to-volume ratio.[39] Most of the APT-based investigations, however, reported a Ti:Mo ratio in the range of 1.1 to 2.0 inside both atom clusters and nano-sized precipitates of 1 to 5 nm size range,[14,32,34,35,37,39,46] which is in accordance with the composition of a majority of precipitates analyzed in the present study. Earlier studies also indicated that equilibrium (Ti, Mo)C precipitate composition with Ti:Mo ratio of ~ 2 is attained after prolonged aging treatment.[34,35,39]

B. Recovery and Recrystallization

As mentioned earlier, no significant precipitation was noticed during the initial annealing period (up to 7 hours) in the investigated steel (evidenced from the TEM and APT analyses). Therefore, all the major solute elements, namely, Mo, Ti and C, were present in solution at the initial stage of annealing. Now, considering the segregation coefficient (β_i), Mo (β_i = 6.3) and C (β_i = 6.4) have a stronger tendency for segregation at the high- and low-angle grain boundaries in the ferrite.[71] Besides the annihilation and rearrangement of dislocations, recovery of a deformed microstructure involves the diffusion and annihilation of vacancies generated by deformation. Now, the strong interaction between the solute atoms and vacancies can restrict the mobility of those vacancies and the associated recovery. Considering the binding energy between the nearest neighbor solute-vacancy pair, the Ti has a strong attraction for the vacancies, followed by the Mo. On the other hand, the C atoms prefer to occupy the interstitial sites next to the vacancy and form carbon-vacancy complexes in the ferrite.[72] Also, as C has a strong tendency to segregate to the dislocations and boundaries inside a deformed structure, the increase in the C concentration in solution during cold rolling (as previously mentioned) will accentuate this effect. Therefore, it is postulated that a strong solute-drag effect exerted by C, Mo and Ti may have retarded the recovery and recrystallization during the initial stage of annealing.

As Ti, Mo and C came out of the solution (Figure 10(e)) to form the atom clusters and precipitates, the solute-drag effect on the different boundaries, dislocations and vacancies was reduced significantly. Consequently, the rate of softening by recovery and recrystallization increased over the annealing during the annealing period of 6 to 8 hours (Figure 4). The coarsening of the pre-existing precipitates at the boundaries also allowed recrystallization to some extent.

The proliferation in the number density of fine precipitates between 7 and 8 hours of annealing engendered a very high pinning force on the remaining dislocations and sub-boundaries and retarded further recrystallization as well as grain growth processes of the matrix till 24 hours of annealing. Thus, a partially recrystallized fine grain structure was obtained even after 24 hours of annealing. Although these precipitates coarsened and became incoherent during annealing, they continued to exert a strong pinning effect. However, besides the precipitate pinning effect, the solute drag effect also played a crucial role in retarding the recrystallization. Despite the low C and Ti contents in the matrix, sufficient Mo remained in solution to impose solute drag and resist the process of recrystallization.

Due to the sufficiently small lattice misfit between (Ti, Mo)C and ferrite along the interface (~ 4.8 pct)[25,73] and a high elastic modulus of (Ti, Mo)C (E = 481 GPa and G = 200 GPa[74]), as well as low diffusivity of Mo along with limited solubility of C in the matrix, these precipitates are more resistant to coarsening (compared to the other microalloy precipitates, such as TiC, Mo_2C, VC, etc). Therefore, the (Ti, Mo)C precipitates offer a more effective retardation of recrystallization and grain growth, along with superior precipitation hardening compared to the other microalloy precipitates.

C. Mechanical Response of Annealing

The marginal increase in the hardness during 6 to 8 hours of annealing (Stage II) is attributable to the following two opposing contributions: (1) softening on account of matrix recrystallization and the associated drop in dislocation density; (2) hardening due to the freshly nucleated partially coherent fine precipitates. The dominance of the latter over the former explains the observed increase in hardness. Additionally, the involvement of different mechanisms in the dislocation-precipitate interaction upon tensile straining has been examined by TEM analysis (Figures 12(a) through (f)). The AR sample exhibited high dislocation density and a limited number of precipitates (Figure 12(a)). In the 6 hours annealed sample, a double-lobe contrast arising out of coherency strain was found inside the fine precipitates (as indicated by the thick yellow arrows in Figure 12(b)). The coherency strain contrast confirms that the nano-precipitates possess a coherent or semi-coherent interface with the matrix. Several studies on Ti–Mo steels recognized the formation of a disc-shaped embryo followed by nanosized precipitates in low C steels, with the interfaces being either coherent or semi-coherent with the ferrite matrix[26,28,30,35,39,47,75] having habit planes parallel to {100} planes of BCC-ferrite. The nano-scale precipitates and ferrite matrix showed coherent interfaces parallel to the habit plane, but incoherent interfaces perpendicular to the habit plane.[47,75] Coherent or semi-coherent interfaces between precipitate and matrix are necessary requirements for dislocation-shearing of particles.[37,75,76] Therefore, precipitate shearing mechanism is expected to operate at the very early stage of (Ti, Mo)C precipitation.[35,37,75,76] Dislocation looping around the coarser precipitates in the same sample is marked by the red arrows in Figure 12(c). In contrast, the 8 hours annealed sample revealed only strain contrast but no evidence of dislocation looping (Figure 12(d)). Dislocation looping around the precipitates dominated during the deformation of 24 hours annealed sample (Figures 12(e) and (f)).
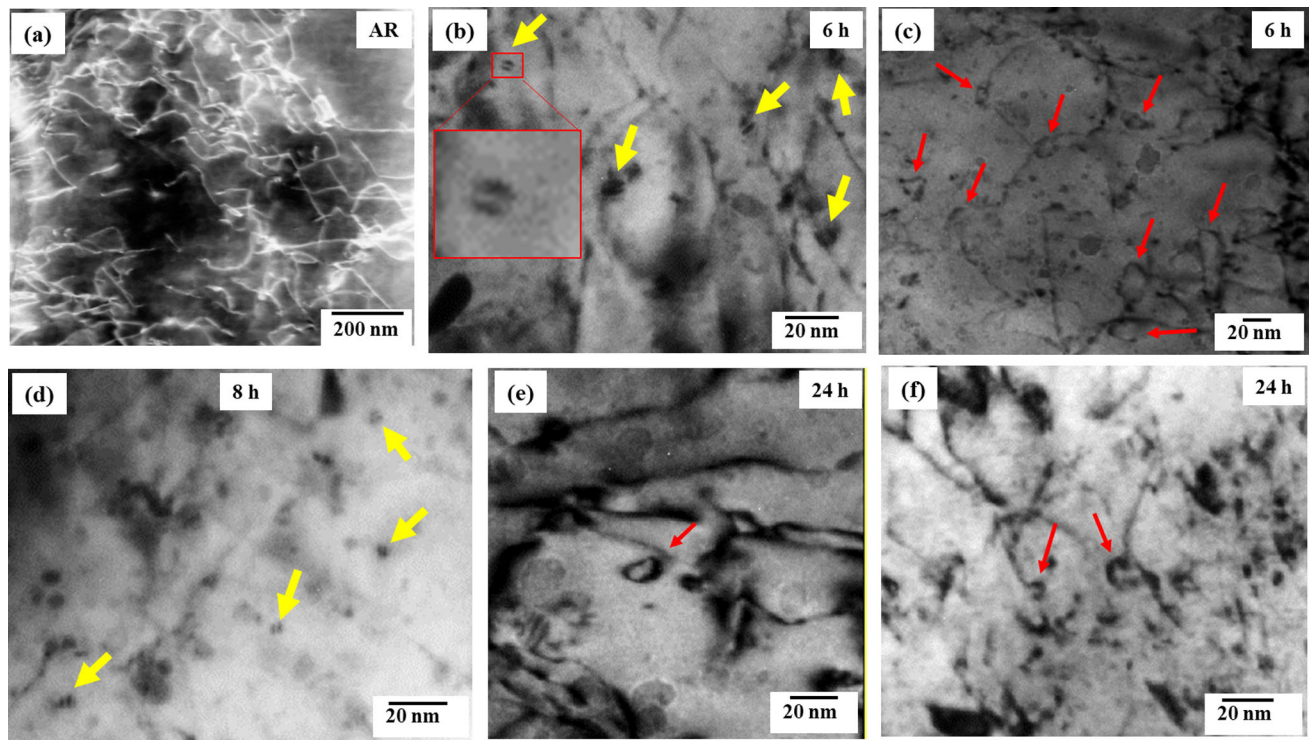
Fig. 12—Dislocation-precipitate interaction upon tensile straining of (*a*) AR and annealed for (*b*) and (*c*) 6 h, (*d*) 8 h, and (*e*) and (*f*) 24 h samples.

It is to be noted that the 8 h annealed sample exhibited yield point elongation, a phenomenon which was not significant in all the other annealed samples (Table II). Yield point phenomenon is governed not only by free interstitial C and N solute contents (associated with the formation of the Cottrell atmosphere at the dislocation core and the corresponding Cottrell locking)[77] and mobile dislocation density,[78] but also by coherent precipitates present in the microstructure. The resistance offered by the coherent nano-sized precipitates on the dislocation movement and the intermittent shearing of those precipitates by the traversing dislocations contribute significantly to yield point phenomenon.[79,80] The presence of abundant fine, partially coherent precipitates in the 8 hours annealed sample, and their associated shearing, is thus expected to have played a prominent role in the observed yield point elongation.

It is to be mentioned in this context that a similar study was carried out on a conventional Nb–V–Ti added steel to compare the role of these microalloying elements on recrystallization kinetics (scope of a separate study to be reported afterwards). In the case of conventional microalloyed steel, almost complete recrystallization was achieved after just 4 hours of annealing at the same temperature, exhibiting a much coarser grain structure (~18 μm). In that steel, the majority of microalloy precipitation occurred early (within 2 h of annealing) and annealing at 873 K (600 °C) for 4 hours resulted in significant coarsening of the precipitates (average size 39.2 ± 8.2 nm). Thus, stable (Ti, Mo)C precipitates can effectively retard the recrystallization and grain growth

in Ti and Mo containing steel compared to more conventional microalloyed steels. The final mechanical properties achieved are certainly at the higher side of a cold-rolled and annealed steel with fully ferrite matrix. The effect of prolonged annealing (for > 24 hours) on the further recrystallization and grain growth in Ti, Mo containing steel has not been studied here as it is not of industrial relevance. This aspect can certainly be studied in future.

V. CONCLUSIONS

The 60 pct cold-rolled sample of Ti–Mo-grade ferritic steel was annealed at 873 K (600 °C) for different durations (2 to 24 hours). The following major conclusions can be derived:

1. During the course of annealing, the steel showed severe retardation of ferrite recrystallization, finely recrystallized grains and high hardness. About 60 pct recrystallization with an average grain size of 8.8 μm was achieved after annealing for 24 hours.
2. Recovery and recrystallization phenomena during annealing took place in three stages:

   (I) Gradual recovery up to 6 hours due to the solute-drag effect along with the precipitate pinning effect. Dissolution of the cementite particles (and a part of the alloy carbide) during cold rolling increased the solute content in the matrix.

(II) Partial recrystallization from 6 to 8 hours due to (1) the decrease in solute-drag associated with the formation of numerous atom clusters (6 to 7 hours) and nano-sized (< 10 nm) precipitates (7 to 8 hours) along with (2) the coarsening of pre-existing precipitates on the boundaries through pipe diffusion.

(III) Retardation of further recrystallization and grain-growth beyond 8 hours by the strong pinning effect of nano-sized precipitates.

3. Retardation of further recrystallization and grain-growth beyond 8 hours by the strong pinning effect of nano-sized precipitates.

4. The 8 hours annealed sample having a partially recrystallized microstructure containing numerous, fine, partially coherent (Ti, Mo)C precipitates along with fine recrystallized ferrite grains manifested the best combination of strength (821 MPa UTS) and ductility (16.5 pct total elongation).

5. Extensive yield point elongation (4 pct) noticed in 8 h annealed sample can be ascribed to the combined effect of shearing of nano-sized precipitates by the dislocations along with Cottrell locking of dislocations by the solute atoms. Such a high yield point elongation can be of concern for automotive outer body application and therefore future studies may be carried out at 873 K (600 °C) for other annealing durations (between 8 and 24 hours, or even > 24 hours).

CONFLICT OF INTEREST

On behalf of all authors, the corresponding author states that there is no conflict of interest

APPENDIX

CALCULATION OF DISLOCATION DENSITY FROM X-RAY DIFFRACTION

The dislocation density was calculated from x-ray diffraction data using modified Williamson–Hall method, and the expression is given by Eq. [a1][81,82]:

$$\rho = \frac{2\sqrt{3} <\varepsilon^2>^{\frac{1}{2}}}{(D \times b)} \quad [a1]$$

where $<\varepsilon^2>^{\frac{1}{2}}$ and D are the micro-strain and crystallite size, respectively, which were calculated from the intercept and slope of the Williamson–Hall plot, and b is the Burgers vector. In our study the calculated dislocation density of S1 steel varied in the range of 1.3×10^{15} m^{-2} to 2.2×10^{15} m^{-2}.

REFERENCES

1. T. Gladman: *The Physical Metallurgy of Microalloyed Steels*, Institute of Materials, London, 1997.
2. K. Hulka: *Mater. Sci. Test. Inform. Ii*, 2005, vols. 473–474, pp. 91–102.
3. C.I. Garcia, M. Hua, K. Cho, and A.J. DeArdo: *Metall. Ital.*, 2009, vol. 101, pp. 35–42.
4. Nina Fonstein: *Advanced High Strength Sheet Steels*, 2015.
5. S.M. Hasan, A. Haldar, and D. Chakrabarti: *Mater. Sci. Technol.*, 2012, vol. 28, pp. 823–28.
6. X. Mao, X. Huo, X. Sun, and Y. Chai: *J. Mater. Process. Technol.*, 2010, vol. 210, pp. 1660–66.
7. A.C.T.M. Van Zwieten and J.H. Bulloch: *Int. J. Press. Vessel. Pip.*, 1993, vol. 56, pp. 1–31.
8. H. Hou, Q. Chen, Q. Liu, and H. Dong: *J. Mater. Process. Technol.*, 2003, vol. 137, pp. 173–76.
9. A. Vinogradov: *J. Mater. Sci.*, 2007, vol. 42, pp. 1797–1808.
10. A. Di Schino and J.M. Kenny: *Mater. Lett.*, 2003, vol. 57, pp. 3182–85.
11. A. Karmakar, M. Ghosh, and D. Chakrabarti: *Mater. Sci. Eng. A*, 2013, vol. 564, pp. 389–99.
12. A. Karmakar, M. Mandal, A. Mandal, M. Basiruddin, S. Mukherjee, and D. Chakrabarti: *Metall. Mater. Trans. A*, 2016, vol. 47A, pp. 268–81.
13. K. Kamibayashi, Y. Tanabe, Y. Takemoto, I. Shimizu, and T. Senuma: *ISIJ Int.*, 2012, vol. 52, pp. 151–57.
14. Y. Funakawa, T. Shiozaki, K. Tomita, T. Yamamoto, and E. Maeda: *ISIJ Int.*, 2004, vol. 44, pp. 1945–51.
15. H.L. Yi, Z.Y. Liu, G.D. Wang, and D. Wu: *J. Iron Steel Res. Int.*, 2010, vol. 17, pp. 54–58.
16. Y. Li, J.A. Wilson, A.J. Craven, P.S. Mitchell, D.N. Crowther, and T.N. Baker: *Mater. Sci. Technol.*, 2007, vol. 23, pp. 509–18.
17. T.N. Baker, Y. Li, J.A. Wilson, A.J. Craven, and DN Crowther: *Mater. Sci. Technol.*, 2004, vol. 20, pp. 720–30.
18. T.P. Wang, F.H. Kao, S.H. Wang, J.R. Yang, C.Y. Huang, and H.R. Chen: *Mater. Lett.*, 2011, vol. 65, pp. 396–99.
19. B.K. Show, R. Veerababu, R. Balamuralikrishnan, and G. Malakondaiah: *Mater. Sci. Eng. A*, 2010, vol. 527, pp. 1595–1604.
20. M.P. Rao, V.S. Sarma, and S. Sankaran: *Mater. Sci. Eng. A*, 2013, vol. 568, pp. 171–75.
21. M. Charleux, W.J. Poole, M. Militzer, and A. Deschamps: *Metall. Mater. Trans. A*, 2001, vol. 32A, pp. 1635–47.
22. V.S.A. Challa, W.H. Zhou, R.D.K. Misra, R. O'Malley, and S.G. Jansto: *Mater. Sci. Eng. A*, 2014, vol. 595, pp. 143–53.
23. M.Y. Chen, M. Gouné, M. Verdier, Y. Bréchet, and J.R. Yang: *Acta Mater.*, 2014, vol. 64, pp. 78–92.
24. Z. Wang, H. Zhang, C. Guo, W. Liu, Z. Yang, X. Sun, Z. Zhang, and F. Jiang: *J. Mater. Sci.*, 2016, vol. 51, pp. 4996–5007.
25. J.H. Jang, C.H. Lee, Y.U. Heo, and DW Suh: *Acta Mater.*, 2012, vol. 60, pp. 208–17.
26. P. Gong, X.G. Liu, A. Rijkenberg, and W.M. Rainforth: *Acta Mater.*, 2018, vol. 161, pp. 374–87.
27. C.Y. Chen, C.C. Chen, and J.R. Yang: *Mater. Charact.*, 2014, vol. 88, pp. 69–79.
28. Z. Wang, H. Zhang, C. Guo, Z. Leng, Z. Yang, X. Sun, C. Yao, Z. Zhang, and F. Jiang: *Mater. Des.*, 2016, vol. 109, pp. 361–66.
29. Z. Wang, X. Sun, Z. Yang, Q. Yong, C. Zhang, and Z. Li: *Mater. Sci. Eng.*, 2013, vol. 573, pp. 84–91.

30. S. Dhara, R.K.W. Marceau, K. Wood, T. Dorin, I.B. Timokhina, and P.D. Hodgson: *Mater. Sci. Eng. A*, 2018, vol. 718, pp. 74–86.
31. Z. Wang, H. Chen, Z. Yang, and F. Jiang: *Metall. Mater. Trans. A*, 2018, vol. 49A, pp. 1455–59.
32. J. Wang, P.D. Hodgson, I. Bikmukhametov, M.K. Miller, and I. Timokhina: *Mater. Des.*, 2018, vol. 141, pp. 48–56.
33. F.Z. Bu, X.M. Wang, S.W. Yang, C.J. Shang, and R.D.K. Misra: *Mater. Sci. Eng.*, 2015, vol. 620, pp. 22–29.
34. I. Bikmukhametov, H. Beladi, J. Wang, P.D. Hodgson, and I. Timokhina: *Acta Mater.*, 2019, vol. 170, pp. 75–86.
35. S. Mukherjee, I.B. Timokhina, C. Zhu, S.P. Ringer, and P.D. Hodgson: *Acta Mater.*, 2013, vol. 61, pp. 2521–30.
36. J. Hu, L. Du, H. Xie, F. Dong, and R.D.K. Misra: *Mater. Des.*, 2014, vol. 60, pp. 302–09.
37. L. Cheng, Q. Cai, B. Xie, Z. Ning, X. Zhou, and G. Li: *Mater. Sci. Eng. A*, 2016, vol. 651, pp. 185–91.
38. Y.W. Kim, S.W. Song, S.J. Seo, S. Hong, and C.S. Lee: *Mater. Sci. Eng. A*, 2013, vol. 565, pp. 430–38.
39. S. Mukherjee, I. Timokhina, C. Zhu, S.P. Ringer, and P.D. Hodgson: *J. Alloys Compd.*, 2017, vol. 690, pp. 621–32.
40. I. Timokhina, M.K. Miller, J. Wang, H. Beladi, P. Cizek, and P.D. Hodgson: *JMADE*, 2016, vol. 111, pp. 222–29.
41. L. Cheng, Y. Chen, Q. Cai, W. Yu, G. Han, E. Dong, and X. Li: *Mater. Sci. Eng. A*, 2017, vol. 698, pp. 117–25.
42. N. Kamikawa, Y. Abe, G. Miyamoto, and Y. Funakawa: *ISIJ Int.*, 2014, vol. 54, pp. 212–21.
43. K. Zhang, Z. Li, Z. Wang, X. Sun, and Q. Yong: *J. Mater. Res.*, 2016, vol. 31, pp. 1254–63.
44. C. Chen, J. Yang, C. Chen, and S. Chen: *Mater. Charact.*, 2016, vol. 114, pp. 18–29.
45. C. Chen, S. Chen, C. Chen, and J. Yang: *Mater. Sci. Eng. A*, 2015, vol. 634, pp. 123–33.
46. Y. Huang, A. Zhao, X. Wang, X. Wang, J. Yang, J. Han, and F. Yang: *Met. Mater. Trans. A*, 2016, vol. 47A, pp. 450–60.
47. J. Wang, M. Weyland, I. Bikmukhametov, M.K. Miller, P.D. Hodgson, and I. Timokhina: *Scr. Mater.*, 2019, vol. 160, pp. 53–57.
48. N. Kamikawa, K. Sato, G. Miyamoto, M. Murayama, N. Sekido, K. Tsuzaki, and T. Furuhara: *Acta Mater.*, 2015, vol. 83, pp. 383–96.
49. Y.W. Kim, J.H. Kim, S.-G. Hong, and C.S. Lee: *Mater. Sci. Eng. A*, 2014, vol. 605, pp. 244–52.
50. D. Chakrabarti, C. Davis, and M. Strangwood: *Mater. Charact.*, 2007, vol. 58, pp. 423–38.
51. W. Sha, L. Chang, G.D.W. Smith, L. Cheng, and E.J. Mittemeijer: *Surf. Sci.*, 1992, vol. 266, pp. 416–23.
52. J. Takahashi, T. Tarui, and K. Kawakami: *Ultramicroscopy*, 2009, vol. 109, pp. 193–99.
53. E.A. Marquis and J.M. Hyde: *Mater. Sci. Eng. R*, 2010, vol. 69, pp. 37–62.
54. A. Biswas, D.J. Siegel, C. Wolverton, and D.N. Seidman: *Acta Mater.*, 2011, vol. 59, pp. 6187–6204.
55. A. Biswas, D.J. Siegel, and D.N. Seidman: *Acta Mater.*, 2014, vol. 75, pp. 322–36.
56. K.R. Gadelrab, G. Li, and M. Chiesa: *J. Mater. Res.*, 2012, vol. 27, pp. 1573–79.
57. ASTM Int. and ASTM: *Astm*, 2009, pp. 1–27.
58. G. Jha, A. Haldar, M.S. Bhaskar, and T. Venugopalan: *Mater. Sci. Technol.*, 2011, vol. 27, p. 1131.
59. F.J. Humphreys: *J. Mater. Sci.*, 2001, vol. 36, pp. 3833–54.
60. A. Sarkar, S. Sanyal, T.K. Bandyopadhyay, and S. Mandal: *Mater. Charact.*, 2017, vol. 134, pp. 213–24.
61. H.W. Yen, C.Y. Huang, and J.R. Yang: *Scr. Mater.*, 2009, vol. 61, pp. 616–19.
62. M.F. Ashby and R. Ebeling: *Trans. Metall. Soc. AIME*, 1966, vol. 236, pp. 1396–1403.
63. J.G. Cowie and F.R. Tuler: *Mater. Sci. Eng. A*, 1991, vol. 141, pp. 23–37.
64. M.K. Miller and M.G. Burke: *J. Nucl. Mater.*, 1992, vol. 195, pp. 68–82.
65. S. Zajac: *Mater. Sci. Forum*, 2005, vols. 500–501, pp. 75–86.
66. P. Klugkist and C. Herzig: *Phys. Stat. Sol.*, 1995, vol. 148, pp. 413–21.
67. S. Murphy and J.A. Whiteman: *Met. Sci. J.*, 1970, vol. 4, pp. 58–62.
68. H.W. Yen, P.Y. Chen, C.Y. Huang, and J.R. Yang: *Acta Mater.*, 2011, vol. 59, pp. 6264–74.
69. J.H. Jang, C. Lee, H.N. Han, H.K.D.H. Bhadeshia, D. Suh, J.H. Jang, C. Lee, H.N. Han, H.K.D.H. Bhadeshia, and D. Suh: *Mater. Sci. Technol.*, 2013, vol. 29, pp. 1074–79.
70. D. Huang, J. Yan, and X. Zuo: *Mater. Charact.*, 2019, vol. 155, p. 109786.
71. J. Seol, S. Na, B. Gault, J. Kim, J. Han, C. Park, and D. Raabe: *Sci. Rep.*, 2017, vol. 7, pp. 1–9.
72. T. Kresse, C. Borchers, and R. Kirchheim: *Scr. Mater.*, 2013, vol. 69, pp. 690–93.
73. O.Y. Kontsevoi, A.J. Freeman, and G.B. Olson: in *Proc. 30th Annu. SRG Meet. Evanston.*
74. D. Edstrom, D.G. Sangiovanni, L. Hultman, I. Petrov, J.E. Greene, and V. Chirita: *Acta Mater.*, 2018, vol. 144, pp. 376–85.
75. Z. Xiong, I. Timokhina, and E. Pereloma: *Prog. Mater. Sci.*, 2021, vol. 118, p. 100764.
76. A.J. Ardell: *Metall. Trans. A*, 1985, vol. 16, pp. 2131–65.
77. G.E. Dieter: *Mech. Metall. SI Metr. Ed. McGraw-Hill B. Co*, 1962, vol. 273.
78. E.O. Hall: *Yield Point Phenomena in Metals and Alloys*, Plenum Press, New York, 1970.
79. A. Zhu: *Acta Mater.*, 1997, vol. 45, pp. 4213–23.
80. D. Thevenet, M. Mliha-Touati, and A. Zeghloul: *Mater. Sci. Eng. A*, 1999, vol. 266, pp. 175–82.
81. Y.H. Zhao, X.Z. Liao, Z. Jin, R.Z. Valiev, and Y.T. Zhu: *Acta Mater.*, 2004, vol. 52, pp. 4589–99, https://doi.org/10.1016/j.actamat.2004.06.017.
82. P. Taylor, G.K. Williamson, and R.E. Smallman, III: *Philos. Mag.*, 1956, vol. 1, pp. 34–46.